Available online at www.sciencedirect.com
SCIENCE DIRECT
Tectonophysics 422 (2006) 99–114
TECTONOPHYSICS
www.elsevier.com/locate/tecto

Characterization of a fractured granitic pluton: P- and S-waves' seismic tomography and uncertainty analysis

D. Martí [a,*], R. Carbonell [a,1], J. Escuder-Viruete [b,2], A. Pérez-Estaún [a,1]

[a] *Department de Geofísica i Tectònica, Institut de Ciències de la Terra "Jaume Almera"-CSIC, 08028 Barcelona, Spain*
[b] *Instituto Geológico y Minero de España, Area de Geología y Geofísica, 28760 Madrid, Spain*

Received 3 February 2006; received in revised form 10 May 2006; accepted 12 May 2006
Available online 3 July 2006

Abstract

A detailed characterization of the physical properties of a granitic pluton, including a three dimensional reconstruction of the fractures network and its surrounding are obtained by high resolution seismic tomography of P and S-waves. The input P- and S-wave travel times were picked from three-component offset and azimuth variable seismic profile (OVSP) acquired in a 500 m deep vertical borehole. The travel time inversion resulted in two three-dimensional P- and S-wave velocity models, and the uncertainty, robustness and sensitivity are estimated by performing a Monte Carlo-type analysis and checkerboard test. This study provides an indicator of the uniqueness of the determined model. The 500 m deep borehole was continuously cored, and extensively surveyed by geophysical techniques. Thus, the detailed surface geological mapping, fracture index logs, borehole televiewer images and P- and S-wave velocities derived from sonic logs, provide solid constraints for the interpretation of the tomographic images. The three-dimensional tomographic images reveal fracture zones mapped at surface that intersect the borehole at different depths and they can be identified in the core descriptions and in the borehole televiewer images. The fractures identified on the cores feature relatively low values for the sonic P- and S-wave velocities, and high values for Poisson's ratio (σ). For single type lithologies, the distribution of Poisson's ratio differentiates fractured and altered granite from fresh unfractured domains within the rock. Poisson's ratios close to 0.3 correlate with fractured volumes consistent with fracture index and sonic logs, otherwise Poisson's ratio values close to 0.25 are related to unaltered and unfractured rock.

Keywords: Granitic pluton; Seismic tomography; Resolution and uncertainty analysis

1. Introduction

Seismic travel time inversion, seismic tomography, has been revealed as one of the most powerful and efficient tools to image the velocity structure of the Earth crust. First introduced by Aki et al. (1975) and Aki and Richards (1980) originally under the name of "Three-Dimensional Inversion", seismic tomography is now a well established technique used in: the determination of the seismic velocity distribution within the Earth; the characterization of the lithospheric and crustal structure, and in detailed and high resolution studies of the shallow subsurface.

The seismic travel time inversion is a non-linear problem thus a large amount of work has been done in modifying the inversion scheme by different approaches,

* Corresponding author. Institut de Cièmcies de la Terra "Jaume Almera" - CSIC, C/ Lluís Solé i Sabarís, s/n 08028 Barcelona, Spain. Tel.: +34 93 4095410; fax: +34 93 4110012.
E-mail addresses: dmarti@ija.csic.es (D. Martí), rcarbo@ija.csic.es (R. Carbonell), j.escuder@igme.es (J. Escuder-Viruete), andres@ija.csic.es (A. Pérez-Estaún).
[1] Tel.: +34 93 4095410; fax: +34 93 4110012.
[2] Tel.: +34 917287242.

0040-1951/$ - see front matter © 2006 Elsevier B.V. All rights reserved.
doi:10.1016/j.tecto.2006.05.012

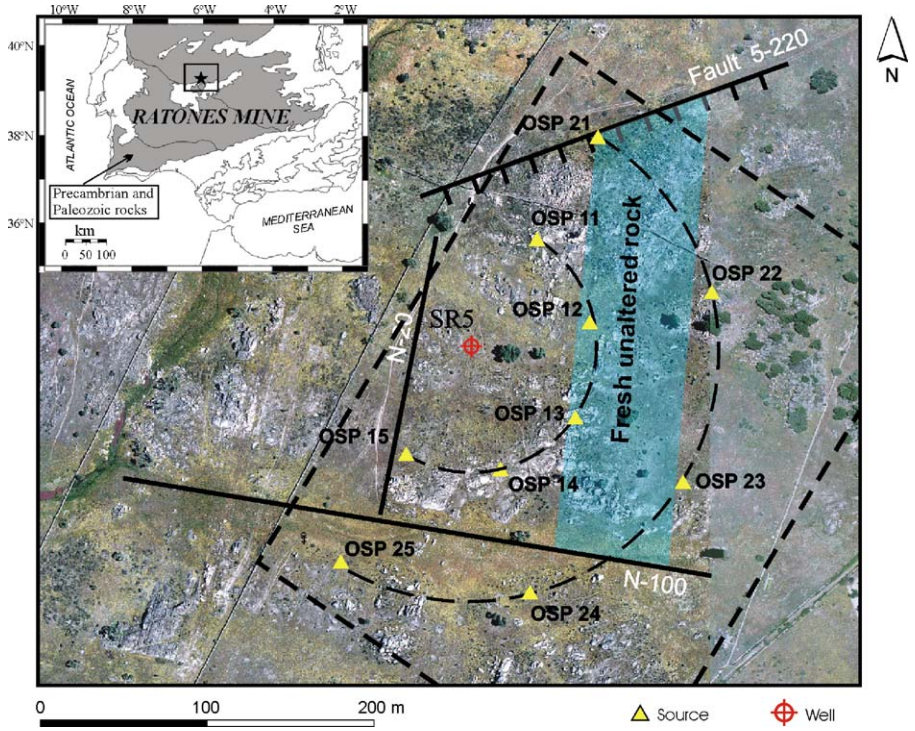

Fig. 1. Simplified map of the geology and aerial photograph of the study area (Ratones Mine, SW of Iberian Peninsula) showing the acquisition geometry (location of the borehole SR5 and location of the source positions, yellow triangles) of the variable azimuth and offset vertical seismic profiles (OVSP). The main fractures mapped at surface are 5-220 fault (which intersects the well at 220 m depth according to the tomograms), N-20 and N-100 (in this case 20 and 100 correspond to the surface measured orientation) faults. It is also observed as a light blue area which is less fractured and altered. The area where the seismic tomography inversion was carried out is indicated with a dashed line.

either by solving the non-linearity by iterative stepwise inversions of the linearized problem, or by the application of non-linear inversion techniques, such as Genetic Algorithms, Monte Carlo or Simulated Annealing methods (Tarantola and Valette, 1982a; Nolet, 1985; Kissling, 1988; Nolet, 1993;). Also in increasing the resolving power either by designing densely recorded experiments, or by introducing in the inversion additional seismic phases such as S and converted arrivals (Carbonell and Smithson, 1994; Benz et al., 1996; Dawson et al., 1999; Carbonell et al., 2002).

Seismic tomography has been used successfully in a broad variety of applications, that include deep and shallow targets. The tomographic inversion of the local earthquake travel time data provides an accurate relocation of the earthquake hypocenters and velocity structures (Pavlis and Booker, 1980; Hawley et al., 1981; Benz and Smith, 1984; Bishop et al., 1985; Chiu et al., 1986; Kissling, 1988; Hole, 1992; Thurber, 1993; Gorbatov et al., 2000). In volcanic areas the definition of low velocity anomalies has suggested the presence of magma chambers (Benz and Smith, 1984; Dawson et al., 1999; Tryggvason et al., 2002). To constrain the crustal and lithospheric velocity structure seismic tomography has been broadly applied (Hole and Zelt, 1995; Zelt and Barton, 1998; Gorbatov et al., 2000; among others). In the shallow subsurface it has been used to detect underground cavities (Madrussani et al., 1999; Flecha et al., 2004), describe the geometry of geological structures such as paleochannels (Azaria et al., 2000) and fault zones

Fig. 2. (a) logs acquired in borehole SR5 as part of the geophysical characterization data acquisition experiment. Vp (i) and Vs (ii) seismic wave velocities derived from the sonic logs. iii) Poison's ratio depth function derived from the Vp and Vs sonic logs (i) and ii) respectively). iv) fracture index as a function of depth. v) and vi) correspond to televiewer images at two different depths. v) corresponds to a highly fractured zone in the borehole, characterized by subhorizontal faulting, note the large concentration of poles (black dots) at the center of the stereonet. vi) corresponds to the borehole televiewer image of a relatively unfractured zone of the borehole. (b) statistical analysis of Poisson's ratio and fracture index for two regions: a fractured area located from 0 to 150 m and a less fractured zone located at the deeper part of the borehole (250–500 m).

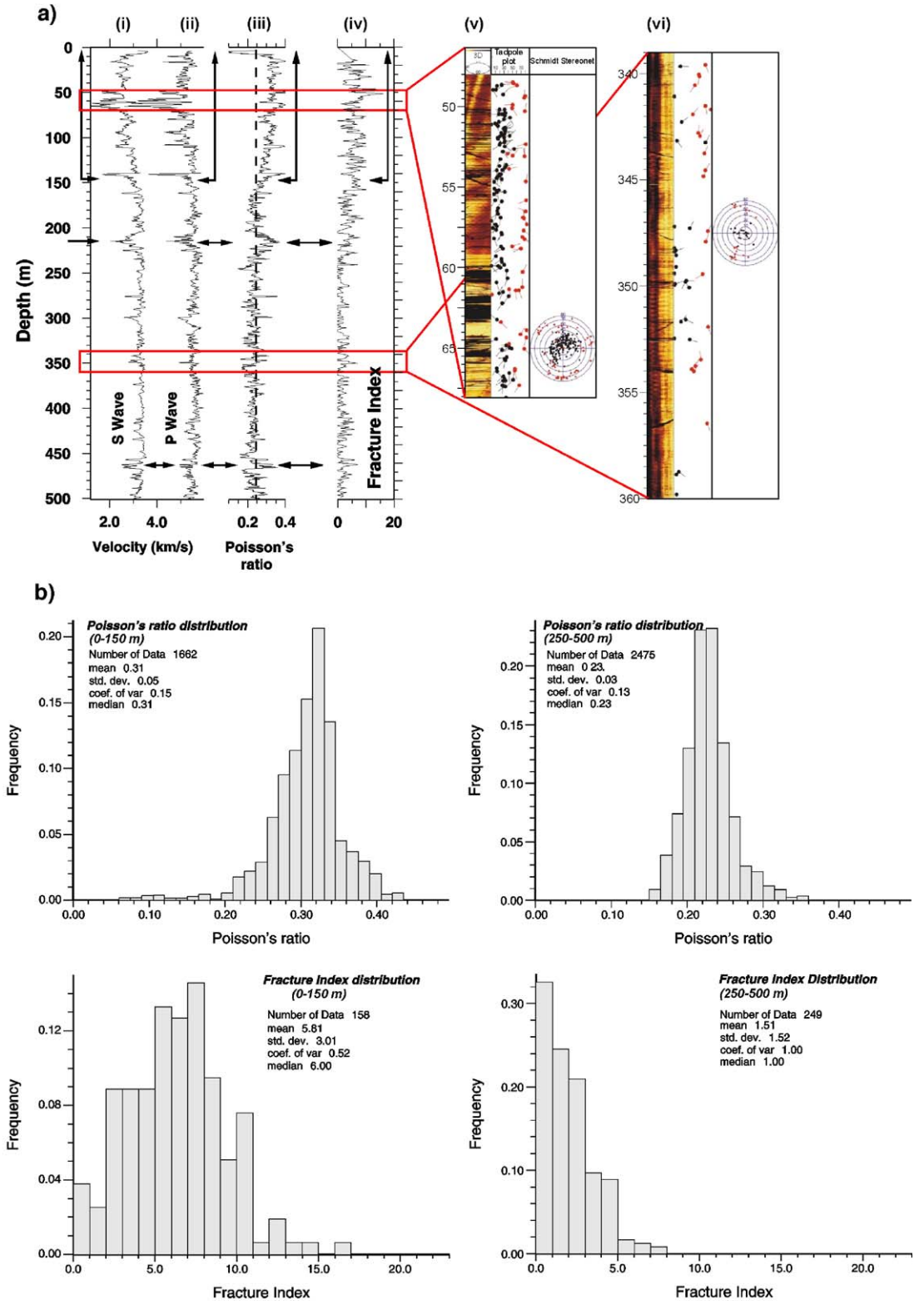
a)
(i)
(ii)
(iii)
(iv)
(v)
(vi)
Depth (m)
S Wave
P Wave
Fracture Index
Velocity (km/s)
Poisson's ratio
Tadpole plot
Schmidt Stereonet
b)
Poisson's ratio distribution
(0-150 m)
Number of Data 1662
mean 0.31
std. dev. 0.05
coef. of var 0.15
median 0.31
Poisson's ratio distribution
(250-500 m)
Number of Data 2475
mean 0.23
std. dev. 0.03
coef. of var 0.13
median 0.23
Fracture Index distribution
(0-150 m)
Number of Data 158
mean 5.81
std. dev. 3.01
coef. of var 0.52
median 6.00
Fracture Index Distribution
(250-500 m)
Number of Data 249
mean 1.51
std. dev. 1.52
coef. of var 1.00
median 1.00
Frequency
Poisson's ratio
Fracture Index

(Morey and Schuster, 1999; Martí et al., 2002a), for reservoir characterization (Milligan and Rector, 2000; Takahashi et al., 2001) and for the characterization of fractured crystalline bodies (Martí et al., 2002b).

This project is part of a mine restoration programme developed by the Spanish radioactive waste management company (ENRESA) with the main objective of calibrating, validating and developing a broad variety of high resolution geophysical techniques applied to the characterization of crystalline rocks. This project included a broad variety of multidisciplinary data acquisition experiments, detailed geological mapping, surface and VSP seismic recording borehole geophysics (logging). The borehole geophysics included different measures of physical properties, as sonic logs (Vp and Vs), fracture index (FI), borehole televiewer, among others. Although, some relevant results have already been published (Escuder-Viruete et al., 2001; Martí et al., 2002a,b; Escuder-Viruete et al., 2003a,b). The joint P- and S-waves' characterization of the study area and a detailed analysis of the resolution and the robustness of the models have not been addressed until this study. The main objective of this study is to constrain the physical properties of a fractured crystalline rock, a granitic pluton. Different seismic techniques can be used to perform the detailed characterization of the rock body, but the seismic tomography reveals as the most adequate methodology to image the fracture zones in a single rock type (granite). Therefore, three-dimensional P- and S-wave velocity models were calculated by inverting P- and S-wave travel times derived from offset and azimuth variable vertical seismic profiles (OVSP) acquired in a 500 m deep borehole. These two velocity models are sensitive to different physical properties of the rock and, moreover, coupled with other geophysical information derived from well logging help to characterize the study area. Resolution and robustness tests validate the resulting velocity models and provide constraints to the best resolved areas around borehole SR5.

2. Geological and geophysical settings

The test site is located within the Albala Granitic pluton in an abandoned Uranium mine. The Albala granitic pluton is a concentric zoned body elongated in the N–S direction located within the Variscan Iberian Massif (Fig. 1). This pluton has been the objective of several interdisciplinary studies (surface geology, borehole investigations, etc.) since early 70's. The Ratones mine is one of several Uranium mines located in the area. It exploited two sub-vertical dikes (27 and 27′), NNE–SSW oriented, between 1955 and 1975 and has since been abandoned.

The ore filled fractures are organized in a pattern, which is consistent with late Variscan strike slip tectonic regime that affected the area of the Albala pluton (Castro, 1986; Sanderson et al., 1991). Additional faults and joints support a complicated deformation pattern. The thickness of individual fault zones can vary between 0.1 and 25 m, though narrow fault zones (<0.5 m) are more frequent. In average, the faults consist of a relatively thin fracture zone and a zone of alteration around it (Escuder-Viruete et al., 2001; and references therein).

A large multidisciplinary data acquisition experiment was carried out in Ratones Mine. Several boreholes were drilled at different locations to sample the subsurface fractures. The wells had continuous core and a variety of logs were acquired to physically characterize the crystalline rock at depth. The fracture index which provides a number of structural discontinuities by unit length of scanline in outcrop and drill cores, was also measured. The detailed surface geology, focused around borehole SR5, mapped fractures at surface (5-220, N-20 and N-100 faults, Fig. 1) and the description of the cores and the logging data have identified prominent fractures at 140, 220, 320 and 460 m depth (faults: 5-140, 5-220, 5-320 and, 5-460 these are named according to the depth position along the borehole, Fig. 2). The study area features at surface, areas with granitic rock outcrop and areas with relatively thin weathered surface layer (Fig. 1).

Highly detailed seismic P- and S-wave velocity depth functions have been estimated from the sonic logs (Fig. 2a). Poisson's ratio (σ) as a function of depth was calculated from these P- and S-wave velocity logs. This physical property, Poisson's ratio, is strongly dependent on composition for a single rock type which is our case. As the drill-hole in entirely within a granitic rock with mostly the same facies, the Poisson's ratio is only dependent on the pore space and fluid content (fractures and alteration). Therefore, variations of σ will be indicative of the degree of fracturing, especially fluid filled fractures. In approximately constant lithologies, variations in σ are often considered responsible for amplitude versus offset (AVO) anomalies in seismic reflection sections (Castagna and Backus, 1993; Hilterman et al., 2000) and used for reservoir characterization.

In average, relatively low sonic P- and S-wave velocities characterize the first 150 m. A simple statistical analysis of this shallow part demonstrate that these low velocity zones feature relatively high σ (a mean value of 0.31) (Fig. 2b) and high values of the

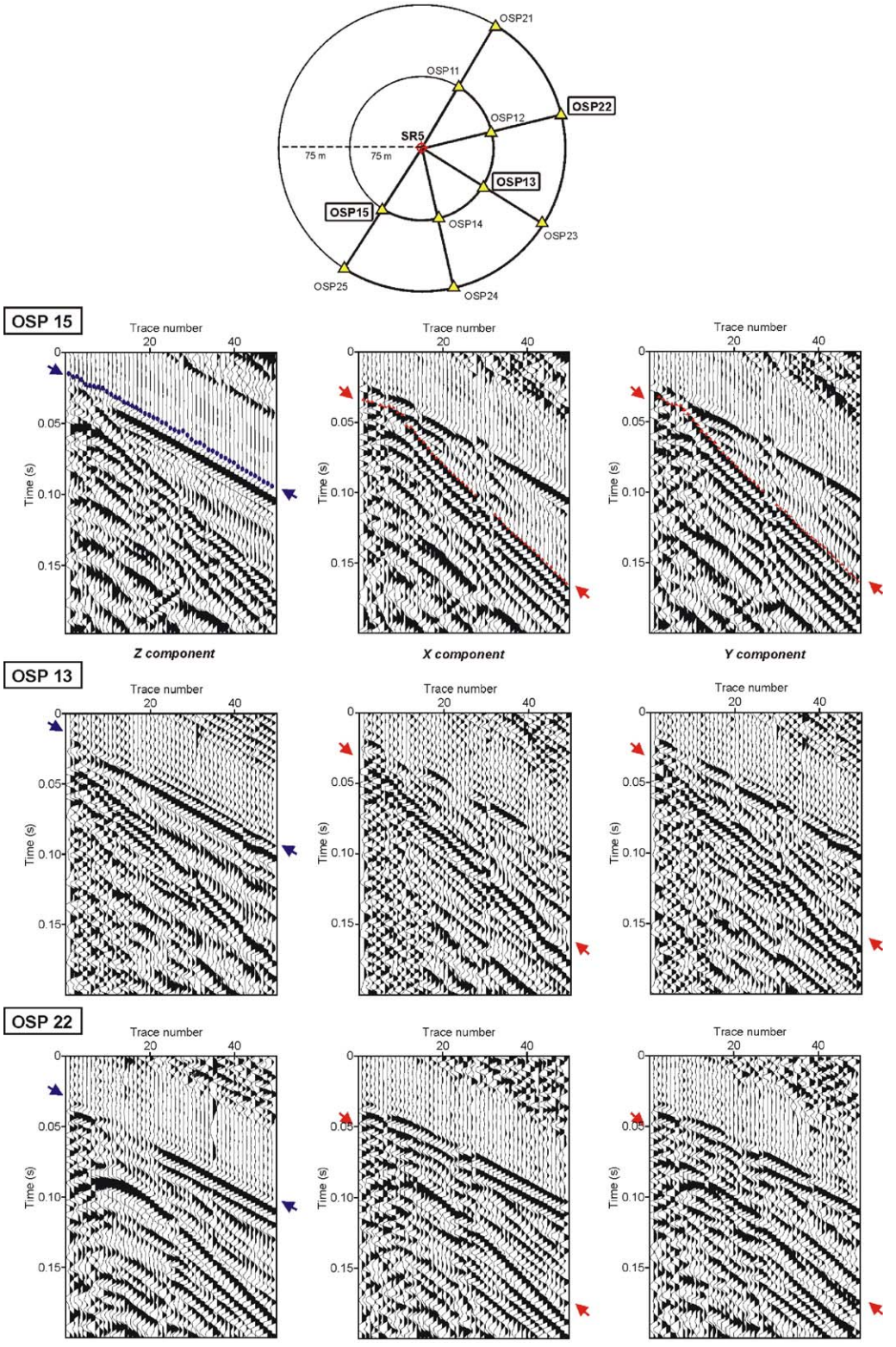

Fig. 3. Three component shot gathers for OSP13, OSP15 and, OSP22 recorded around SR5, illustrating the quality of the data set. The three components are the vertical component and the two horizontals (component *X* oriented EW and component *Y* oriented NS). The blue arrow shows P-wave first arrival, while the S-wave first arrival is marked by a red arrow. An example of the S-wave picking is superimposed for the shot gather OSP15.

fracture index. There is a marked velocity low between 56 and 79 m depth which correlates with a high FI, and the borehole televiewer images display low angle faulting (Fig. 2a). Low velocities are also identified in narrow bands located at, approximately, 215 m and 460 m depth (Fig. 2a). The cores reveal the existence of a fractured zone between 210 and 230 m depth and the existence of an ankerite dyke at approximately 450 m depth. Low seismic velocities (sonic P- and S-wave velocities) correlate with high values of the FI. Descriptions of the drill core and the images of the borehole televiewer support these correlations. High P- and S-wave velocities and $\sigma < 0.25$ correlate with low values of the FI, and zones with less concentration of fractures. The deeper part of the borehole (from 250 to 500 m) is an example of these areas, showing the expected low values of the Poisson's ratio (a mean value of 0.23) and the FI in the statistical analysis (Fig. 2b). The detailed surface geology (Fig. 1), the log information (Fig. 2), the correlations between the logs, the fracture index and, the borehole televiewer images, constitute the boundary constraints for the interpretations of the tomographic images.

3. Seismic data, acquisition, processing and inversion

The borehole SR5, a 500 m deep vertical borehole (Fig. 1) was used to acquire a variable offset and azimuth vertical seismic profiles (OVSP) which consisted in a series of ten vertical seismic profiles; one at 0 m offset; five distributed at 45° angles along half a circumference of 75 m radius centered at the borehole and, the last five were distributed along a second half circumference of 150 m radius centered, also, at the borehole (Fig. 1). The energy generated by a single 22 Ton Vibroseis truck was recorded by a three component borehole geophone (Fig. 3) deployed every 10 m. The source consisted in a band limited zero phase wavelet (after cross correlation) with a frequency content between 15 and 150 Hz. Two sweeps were generated per shot point, both sweeps were diversity stacked before correlation, the time delay between sweeps was such that it provided an effective attenuation of the 50 Hz electrical noise generated by electric power lines. The resulting data set consisted of three shot gathers per shot point (one shot gather per component) a shot gather for the vertical geophone, a second for the EW oriented

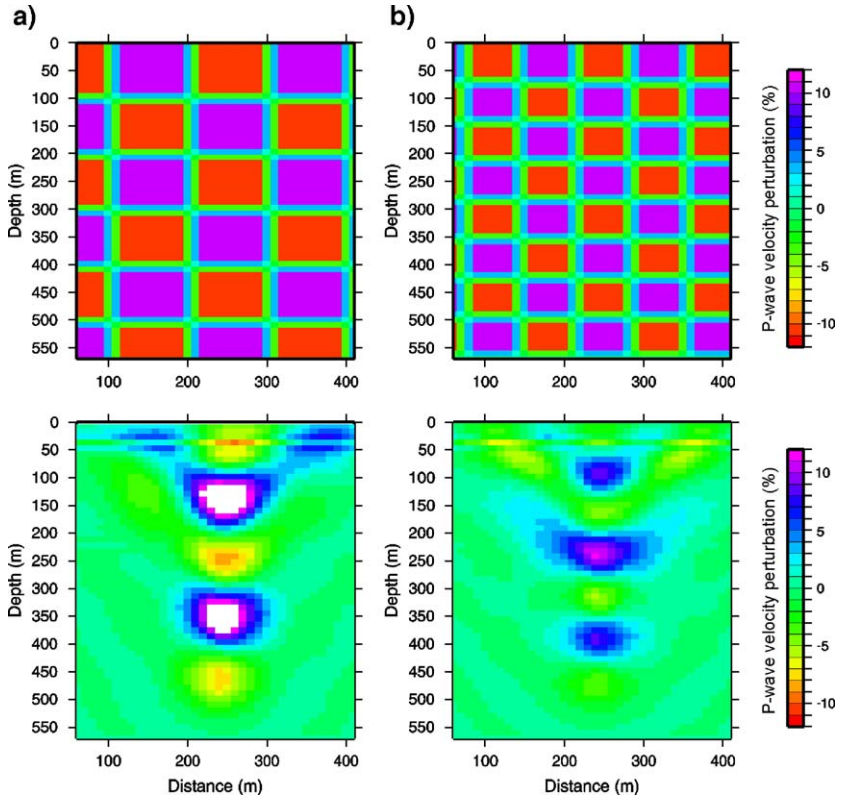

Fig. 4. Checkerboard tests with different cell sizes. This shows the well resolved areas of the model with the given acquisition geometry. (a) cell size of 100 × 100 m, and (b) 70 × 70.

geophone (*X* component) and a third shot gather for the NS oriented geophone (*Y* component) (Fig. 3). The Vibroseis truck used was a compressional source, therefore, all the S-wave energy recorded by the sensors, was most probably generated by conversion at the source location point (Vibroseis point, VP).

The resulting OVSP shot gathers constitute three independent data bases consisting of: vertical component, EW and NS horizontal component. For each data base, the first arrival travel times were digitized and then inverted using well established tomographic inversion algorithm (Tryggvason, 1998). This is an iterative inversion scheme which solves the forward model using finite difference solution of the eikonal equation (Vidale, 1990) and the inversion is performed through a LSQR method (Paige and Saunders, 1982), further details on the mathematics can be found elsewhere (Benz et al., 1996; Tryggvason et al., 2002). As conventional inversion algorithms the data used to obtain the velocity models consisted in the travel time picks and the coordinates of the source and receiver locations, which were acquired during the field operations. The tomographic algorithm requires a 3D grid composed by constant velocity cells through which the travel time front is propagated as a plane wave in each cell. The size of these cells that control the travel time calculations depends on the number of rays traced and their distribution within the velocity model. Martí et al. (2002a) discussed an only preliminary P-wave velocity model derived from P-wave travel times. The first arrivals on the vertical component records are well defined, while S-wave arrivals are more complicated to pick (Fig. 3). Therefore only clearly defined S arrivals were used. The travel time picks corresponding to the S-wave arrivals in the horizontal component shot gathers are not the first phases that can be identified. The S-wave travel time picks must be selected from latter high amplitude waveforms and therefore, these S-wave picks feature higher uncertainties than the P-wave picks. The EW and NS S-wave travel time picks were inverted independently and provide two different velocity models. The existence of two different velocity models could be related to the internal structure of the granitic massif, in particular to fracturing and/or the stress field and provide evidence of seismic anisotropy (Nur, 1971; Crampin, 1985; Crampin and Booth, 1989; Lynn et al.,

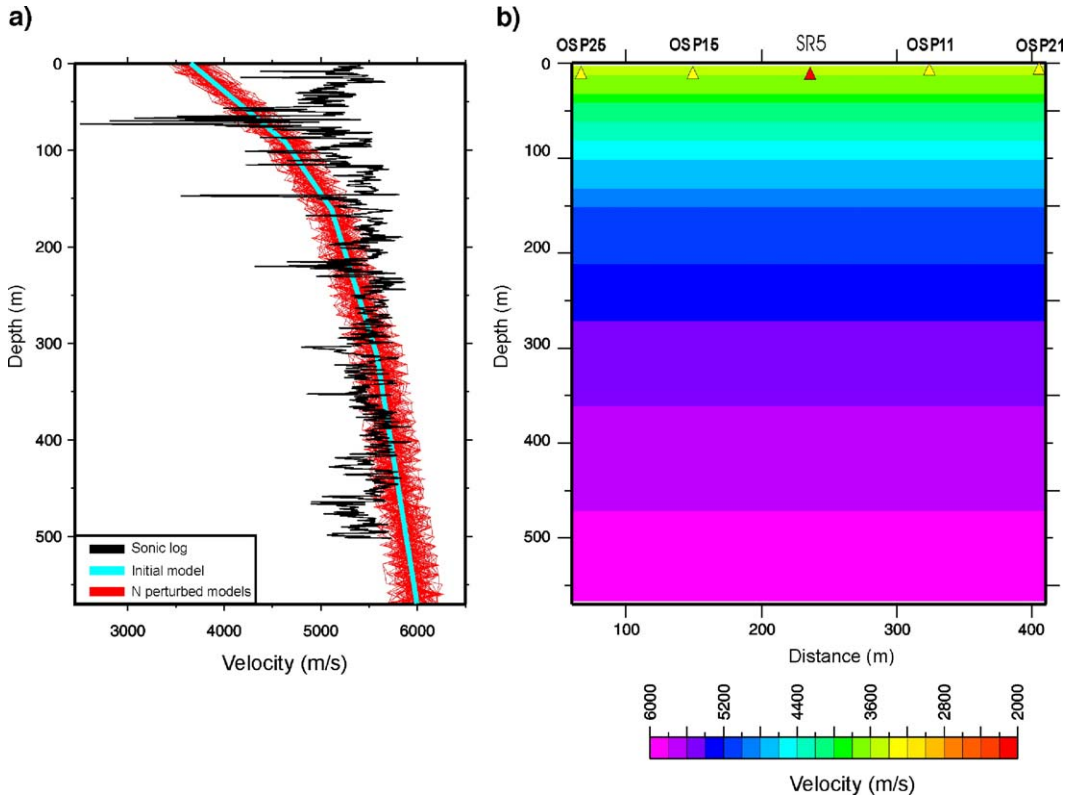

Fig. 5. (a) Simplified 1D initial model (blue line) derived from the Vp sonic log acquired in SR5 (black line). The red lines correspond to the N initial perturbed models used in the Monte Carlo-type analysis that show the dispersion in relation to the unperturbed model. (b) vertical section of the resulting 3D initial velocity model OSP21 to OSP25 passing through the borehole SR5, used in the tomographic inversion.

1996a,b). Nevertheless, in this study the small differences in both velocity models and the relatively large uncertainties in the S-wave travel time picks make it difficult to interpret the differences between the two S-wave velocity models in terms of anisotropy. Thus, an average S-wave velocity model is considered as the most adequate.

4. P- and S-wave tomography and Poisson's ratio

4.1. Resolution and accuracy tests

In order to assure the reliability and quantify the uncertainity of the velocity models derived from the seismic tomography, several tests were carried out. Sensivity tests showed the capacity of the source-receiver geometry of resolving a determined structure by means of synthetic data. A quantification of the uncertainties of the final model which is mandatory for the geological interpretation of the results were also estimated, because it assured the correct correlation between seismic velocities and rock composition.

The checkerboard tests were used, in SR5, to estimate the sensivity of the acquisition geometry and the data set related to the velocity anomalies. These tests constrained the well resolved areas of the model, indicating the size of the anomalies and velocity constrast which can be distinguished with the methodology. The tests performed in Ratones Mine demonstrated that the areas sampled by the ray tracing coincided with the areas recovered by the checkerboard analysis. The velocity anomalies were well imaged at surface and through the entire model, being

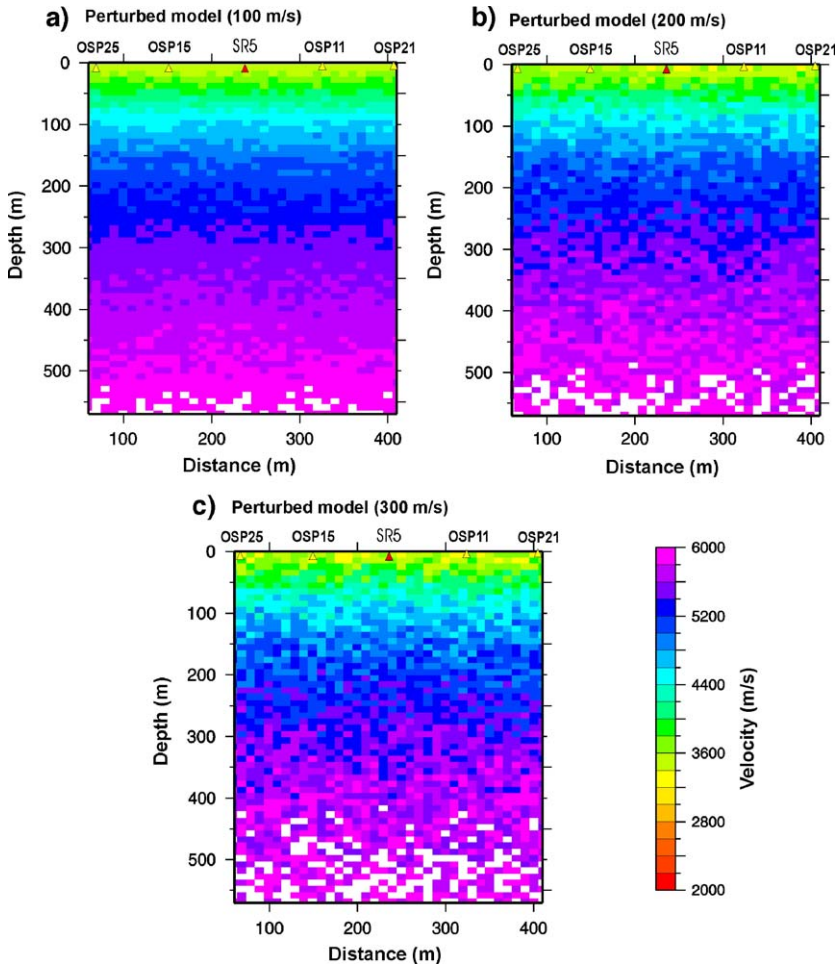

Fig. 6. Vertical sections of the perturbed initial 3D model from OSP21 to OSP25 passing through the borehole SR5 used in the Monte Carlo-type analysis. The random error was added at every cell of the discrete model used in the tomographic inversion. Three different subensembles were built in the study applying different maximum value of the random error in each one. (a) example of the ensemble perturbed ±100 m/s. (b) ±200 m/s and (c) ±300 m/s.

narrower at the base of SR5, displaying an inverse cone shaped area (Fig. 4).

The uncertainties related with the inverse problem were studied by means of the Monte Carlo-type analysis (Tarantola, 1987; Tarantola and Valette, 1982b). In this case, the analysis proceeded inverting N random models with random errors, assuming the equiprobability (1/N) of all of them (Korenaga et al., 2000; Sallarès et al., 2003).

The N different models were simulated from an initial 3D velocity model derived from the geophysical and geological information obtained in SR5. The volume with the highest degree of fracturing is located above 140 m which includes a surface weathered layer of variable thickness. The comparison between the fracture index logs and the sonic logs indicates that this shallow part was characterized by low velocity anomalies. The velocity increases in depth with a high velocity gradient. Below this fractured area, the sonic logs restore the expected mean value (around 5500–5700 m/s) for the unfractured granite in the study area (Martí et al., 2002a,b). The 1D initial model synthesizes the main features observed in the geological and geophysical data set, low seismic velocity at surface increasing quickly at first 150 m, and then, a smoothed velocity gradient to the base of the borehole (Fig. 5). The 3D initial model was obtained extending laterally

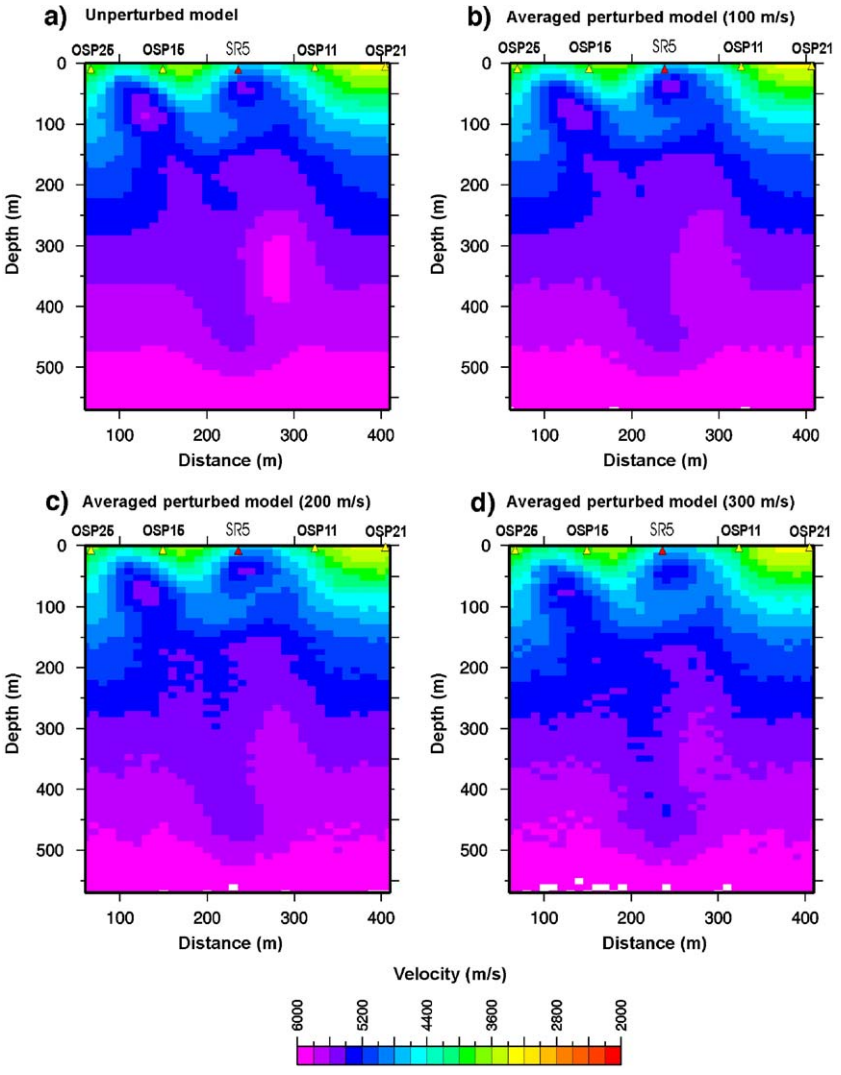

Fig. 7. Vertical sections of the resulting 3D velocity models from OSP21 to OSP25 passing through the borehole SR5 obtained after 6 iterations in the the tomographic inversion. An averaged velocity model for every subensemble is displayed together with an unperturbed model which allows to compare the differences resulted from the random error addition. a) Model obtained from an unperturbed initial model. b), c) and d) Averaged perturbed models with a maximum value of 100 m/s, 200 m/s and 300 m/s, respectively.

and homogeneously this 1D model (Fig. 5). The N initial models of the Monte Carlo ensemble were built by adding a random velocity variation per inversion grid cell to the 3D initial model, creating three different "sub-ensembles" of 35 models each one with a maximum variation of ±100 m/s, ±200 m/s and ±300 m/s respectively (Fig. 6). Errors associated to picking of the first arrivals were also taken into account by adding a random error of ±2 ms to the data set which corresponds approximately to a quarter of the period.

Once all the perturbed initial models were built, a six iteration tomographic inversion process was performed with each of them, according to the acquisition geometry carried out around SR5. All the resulting 3D velocity models were compared with an unperturbed velocity model. This analysis reveals the effects of the different random errors in the final velocity model. In general, all the velocity models of the ensemble resolve the same main features characteristic of the study area (Martí et al., 2002b; Martí, 2004), especially the low velocity anomalies observed at both sides of the SR5 (Fig. 7) that correspond to mapped fracture zones at the surface and on the cores. In order to estimate the uncertainties associated to every subensemble, the mean deviation between every model and an averaged model was calculated (Fig. 8). The results show that the maximum mean deviation obtained, coincides with the models perturbed 300 m/s, featuring uncertainties of about 60 m/s, which represent in average, a 1–2% of the velocity values (Fig. 8). The highest uncertainties are observed in the upper part of the velocity model, coinciding with two high velocity anomalies located beneath the shot points OSP15–OSP25 and between the OSP11 and the borehole SR5 (Figs. 8 and 9). In these areas, the unfractured granite, characterized by high velocity anomalies (up to 5000 m/s), is in contact with the surface weathered layer and the low velocity anomalies (close to 3500 m/s) associated to the fracture zones resulting in a high velocity gradient in the tomographic model. This velocity gradient causes significant

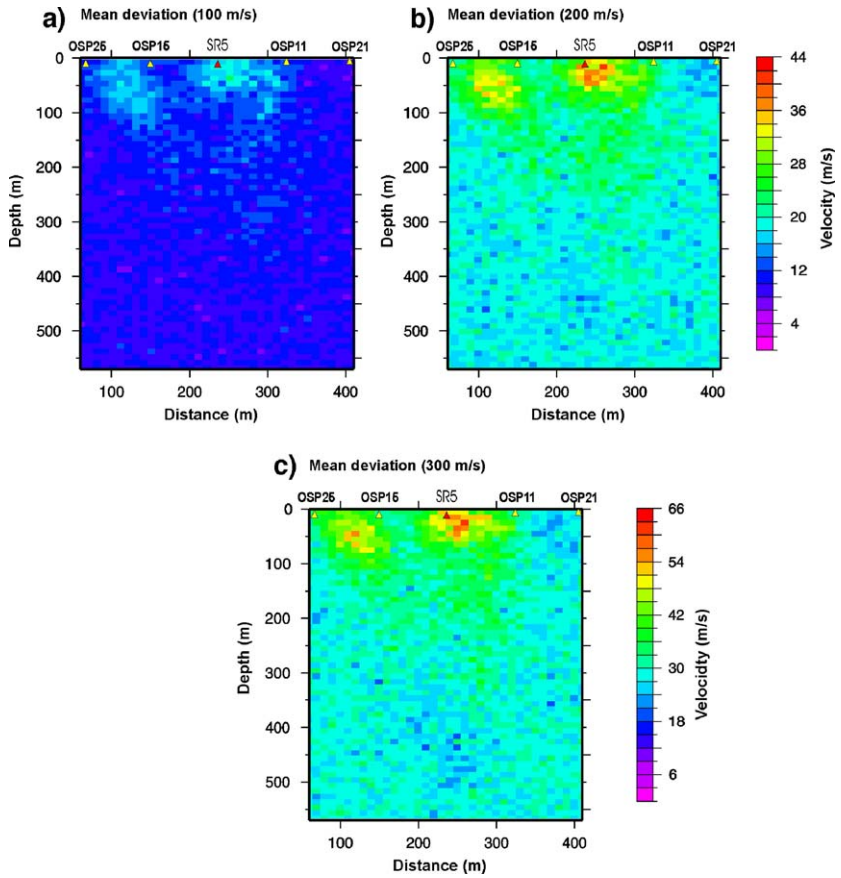

Fig. 8. Velocity uncertainties calculated from the mean deviation of every model respect to an averaged model. The areas with the large uncertainty coincide with high velocity anomalies and a high velocity gradient that causes relatively large changes in the velocity model with small changes in the first arrivals. The estimation of the mean deviation was made for the three subensembles of perturbed models, (a) 100 m/s, (b) 200 m/s and (c) 300 m/s.

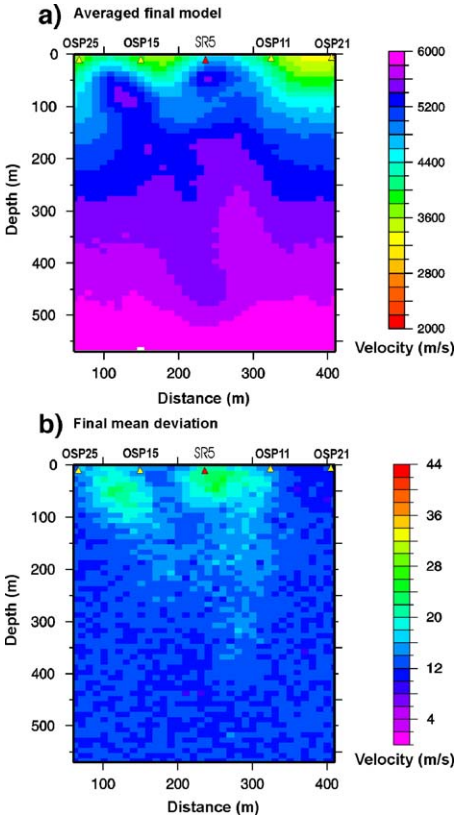

Fig. 9. Synthesis of the results obtained in the accuracy tests made to the data set. (a) averaged velocity model derived from all the models included in the ensemble. (b) mean deviation calculated using all the models of the ensemble.

changes in the velocity model when small changes in the first arrivals (even in the range of the travel time uncertainties) are added.

The results obtained in the 3D velocity model and the mean deviation of the whole ensembles (Fig. 9) assure that the final model have no dependence with the initial model. This is indicative of the robustness of the solutions obtained. The added errors in the travel time picks drive to a final velocity model that still resolves the same structure that were imaged by the unperturbed model suggesting that the solution is close to be unique. Therefore, an averaged velocity model derived from all the resulting models can be used as a starting point in the tomographic inversion to fit the P- and S-wave models that better characterizes the surrounding area of borehole SR5.

4.2. Results of tomographic inversion

The three-dimensional (300×150×500 m) velocity models were calculated using a 10×10×10 m three dimensional grid (Table 1). The resulting P-wave velocity (Fig. 10a) model features a relatively thin (approximately 20 m) top low velocity layer which corresponds with a highly altered surface layer of granite. This low velocity increases up to values approaching 4600 with the top 40 m. At, approximately, 200 m depth the P-wave velocity increases up to 5600–5800 m/s. In detail the model features several velocity anomalies, relatively, low velocities of 4500 m/s near the top of the borehole at 70 m depth and high velocities of 5800–6000 m/s from 250 m up to the base of the borehole (Fig. 10).

The S-wave velocity model that resulted from the inversion of all the travel time picks (Fig. 10b) also indicates, in average, the existence of a sharp gradient at the top from very low velocities (2800 m/s) at 60 m depth up to 3400 m/s at 200 m depth. From 200 m up to the base (500 m) the velocity variation is small in the range of 3600 to 4000 m/s. The S-wave velocity model reveals local high and low velocity anomalies. The S-wave velocity model displays a "Y" shaped high velocity anomaly (of approximately 3800–4000 m/s) the left branch starts at the surface location of OSP25 and the right branch starts at the surface location of OSP11 (Fig. 10b). Note that the low velocity anomaly (2600 m/s) starts at the surface location of OSP15 and intersects the borehole at approximately 170 m depth. Another low velocity anomaly dipping towards the borehole and another that intersects it at 230 m. Both low velocity anomalies appear to coincide at surface with mapped fractures and at the intersection with the borehole with fracture zones identified in the cores.

The Poisson's ratio for isotropic rocks can be estimated by

$$\sigma = \frac{\left(\frac{\alpha}{\beta}\right)^2 - 2}{2\left[\left(\frac{\alpha}{\beta}\right)^2 - 1\right]} \quad (1)$$

Where α and β correspond to the P- and S-wave seismic velocities. σ features a very narrow range centered at

Table 1

SR5 depth	500 m
P-wave first arrivals	488
Cell size forward modelling (m)	1×1×1
Cell size inversion modelling (m)	10×10×10
Initial RMS	0.006631 s
Final RMS	0.001007 s
S-wave first arrivals	451
Cell size forward modelling (m)	1×1×1
Cell size inversion modelling (m)	10×10×10
Initial RMS	0.011119 s
Final RMS	0.002252 s

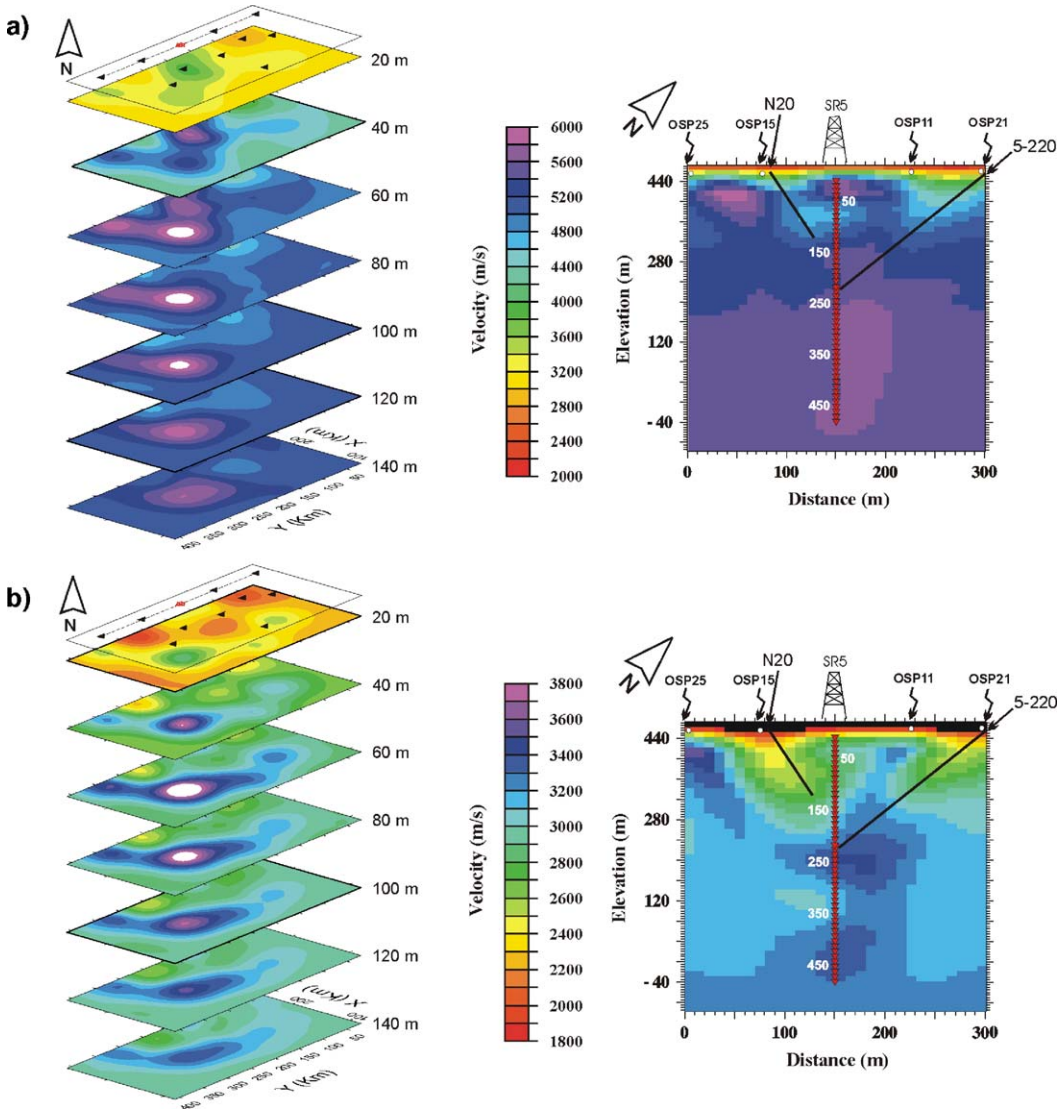

Fig. 10. Velocity field obtained after the inversion of the travel times. (a) P-wave velocity model derived by inversion of P-wave arrivals. Vertical section of the velocity model from OSP21 to OSP25 passing through the borehole SR5. The surface fractures, 5-220 and N-20 faults, are correlated with low velocity anomalies. The volume of unfractured rock is characterized by a high velocity anomaly dipping from the surface towards the borehole, and it intersects the well between 220 to 460 m. (b) velocity model obtained after the inversion of the S-wave arrivals. This velocity model has been calculated as the average of the velocity derived from the S-wave travel time picks of the EW horizontal component recordings and from the S-wave travel time pick NS horizontal component recordings. Vertical section of the velocity model from OSP21 to OSP25 passing through the borehole SR5. The main features identified in the P-wave tomograms (a), 5-220 and N-20 faults even the volume of unfractured rock, are also observed in the S-wave results.

0.25. Poisson's ratio is used to overcome the non-uniqueness of the interpretation of P-wave velocity in terms of rock types (Christensen and Fountain, 1975). For common unaltered and unfractured rock types the Poisson's ratio varies from, approximately, 0.10 to 0.35 (Ji et al., 2002). This variation is related to the composition (density, quartz content…) of the rock. Changes in porosity and fluid content will mainly affect S-wave velocities, thus, fracturing affects this physical property. Therefore, variations in σ when dealing with a single lithology and/or rock type (granite in this study) are indicative of variations in the degree of fracturing (Jones and Holliger, 1997; Goff and Holliger, 1999; Martí et al., 2002b). In consequence, the Poisson's ratio images will differentiate between fractured and unfractured volumes of granite (Figs. 2 and 10).

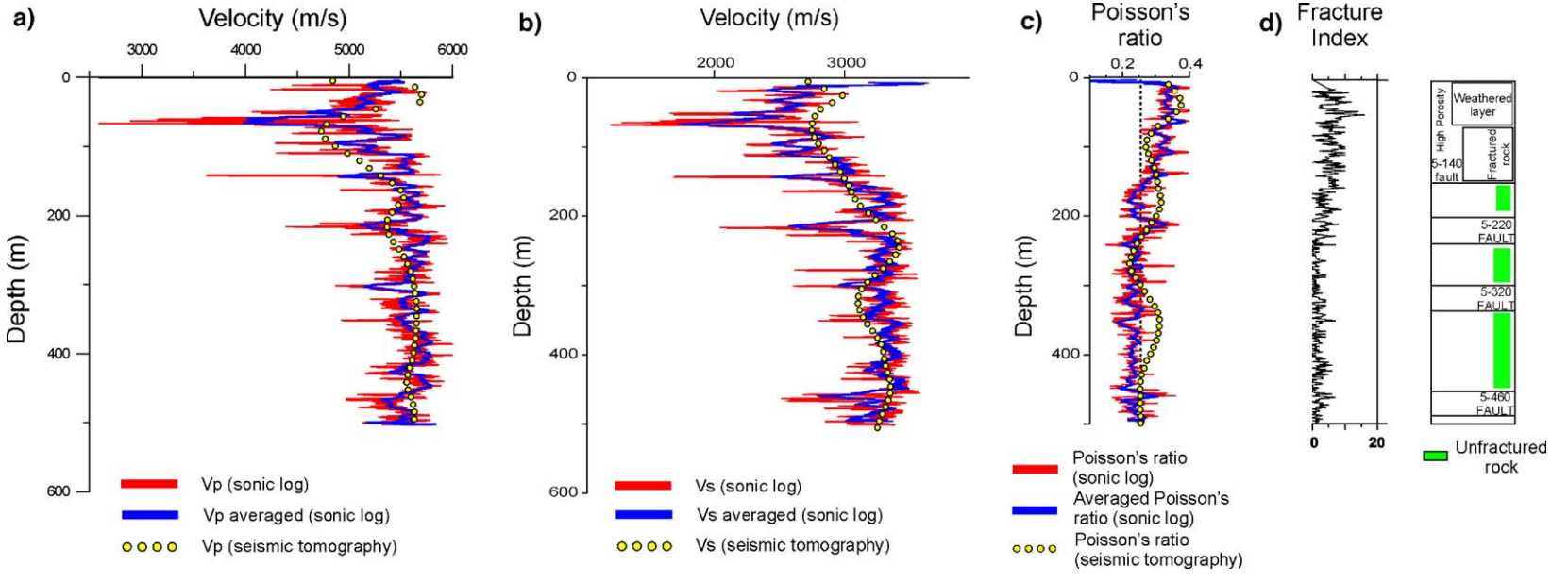

Fig. 11. (a) P-wave seismic velocity logs. The sonic log acquired in the SR5 borehole and the averaged log are plotted by a red and blue continuous lines, respectively. The averaged log has been obtained by averaging over a 3 m sliding window. In dotted yellow line, the P-wave log derived from the seismic tomography velocity model at the SR5 position. On the right side, the qualitative interpretation and the fracture index obtained from the continuous core. (b) S-wave seismic velocity logs. The sonic log acquired in the SR5 borehole and the averaged log are plotted by red and blue continuous lines, respectively. The averaged log has been obtained by averaging over a 3 m sliding window. In dotted line, the S-wave log derived from the seismic tomography velocity model. On the right side, the qualitative interpretation and the fracture index obtained from the continuous core. (c) comparison between the Poisson's ratios obtained from the sonic logs (continuous lines) and the P-wave and S-wave velocities derived from the seismic tomography.

5. Discussion and implications

The information provided by the logs constitutes key constraints for physically reasonable interpretation of the seismic velocity models derived by the tomographic inversion. The available data, in particular the Vp and Vs velocity depth functions derived from the sonics can be directly compared with the Vp and Vs velocities determined by the tomography along the borehole. Nevertheless, the scale of the resolution on both data sets is considerably different. While the logging tool provides a very dense data set, less than meter scale, the tomograms provide velocities every 10 m. The variable sampling of the different techniques makes it difficult to compare and validate all the results obtained in the experiment. For this reason, the sonic and fracture index logs, with a sample rate of 0.20 m, were averaged in order to display a degree of detail comparable with the tomographic images. A relatively narrow, 3 m, sliding window was used for averaging as we wanted to preserve the small scale characteristics of the logs.

The Vp and Vs velocities derived from the sonic logs, the Poison's ratio estimated from them and the FI depth function were compared with the Vp and Vs velocities obtained by the tomographic inversions (Fig. 11). The Vp tomographically derived velocity depth function follows the overall behavior of the Vp derived from the sonic logs. The log velocities from the top of the borehole to 100 m depth feature low values with a minimum located between 50 and 70 m approximately (Fig. 11). This coincides with high values for the FI log which is indicative of fractured areas. The Vp tomographic velocity follows this pattern more smoothly. The tomographic velocity increases at, approximately, 130–170 m depth, indicating a decrease in the degree of fracturing, which is consistent with the Vp log and the FI (Fig. 11). Again, a fracture is indicated by the tomographic Vp between 190 and 240 m depth. This fracture has been described in the core report, and it is also consistent with the FI data. The Vp tomographic velocity reaches values above 5500 m/s, suggesting that from 240 down to the base of the borehole (500 m) granitic rock is fairly fresh and lacks prominent fracturing, except at approximately, 440 m depth, where the Vp decreases (Fig. 11). The core report describes an ankerite dyke at this depth.

The relatively low values for the sonic Vp suggest a fracture zone at, approximately, 300 m depth, which is also apparent in the FI data, and it is not imaged by the tomographic Vp. The seismic data has not been able to image this fracture, probably because it is very thin for the frequency content of the seismic signal to be able to resolve it and the fractured volume is very limited.

From the S-wave velocity model calculated from the horizontal component travel time picks, an S-wave velocity depth function can be derived. In average terms, the velocity depth function provides a low frequency equivalent of Vs log. Up to 140 m depth the velocity depth function displays relatively low velocity values (below 3000 m/s), the minimum value is located at approximately 100 m depth (2700 m/s) (Fig. 11). A change in the velocity gradient is identified at 200 m depth, the velocity starts increasing more rapidly. The S-wave velocity depth function increases up to a maximum at 250 m depth 3200 m/s (Fig. 11). The sampled fracture zone 5-220 located at 220 m depth is only suggested by the change in the velocity gradient. At 320 m depth the velocity function shows a minimum that coincides with the mapped fracture 5-320 (Fig. 11). Beneath this fracture zone the S-wave velocities increase. This increase is most probably due to the decrease in fracturing as suggested by the FI and the interpretation of the P-wave tomographic images. The base of the borehole features also a decrease in the S-wave velocities, probably as a result of the influence of fracture zone 5-460, located at 460 m depth (Fig. 11).

While, logs provide information on the physical properties at a very high depth resolution only on a vertical one dimension, P- and S-waves' tomography provides the physical properties on a three dimensional volume, the resolution scale depends on the acquisition design, but it is usually on the order of meters. Tomographic P- and S-wave velocity–depth functions can be correlated with the sonic and FI logs. They are low pass filtered versions of the logs.

The sonic logs (Vp and Vs), the Poisson's ratio and the fracture index provide the key for a physically reasonable interpretation of the velocity anomalies determined by the seismic tomography (Nur, 1971; Berge et al., 1992; Mukerji and Mavko, 1994; Martí et al., 2002a). A direct correlation can be established between areas with a high porosity (Poisson's ratio, $\sigma > 0.25$) and high fracture index with low velocity anomalies. On the other hand, the Poisson's ratio decreases to $\sigma < 0.25$ in the unfractured parts of the granite (Carmichael, 1982), as well as the fracture index, while the seismic velocities feature high value anomalies.

6. Summary and conclusions

Three-dimensional P- and S-wave velocity models were calculated by the inversion of travel time picks of first arrivals of P- and S-waves of offset and azimuth variable seismic profiles (OVSP) acquired in a 500 m deep vertical borehole drilled in a granitic pluton. The resolution study indicated that the resulting tomographic

model was the optimum that could be achieved by this data set. The uniqueness of the solution was assured because it had non-dependency of the initial model and the added errors in the travel time picks led to the same final model. The surface outcrop of the granitic pluton in the surroundings of the borehole was map in detail by surface geology, and the borehole was surveyed by a number of geophysical techniques, sonic and fracture index logs, borehole televiewer among others. These additional data provide solid constraints for the interpretation of the tomographic images. Low P- and S-wave velocity anomalies identified in the tomographic images correlate with fractures sampled in the cores. These fractures are characterized by relatively low values for the sonic P- and S-wave velocities, and high values for σ. The three-dimensional tomographic images reveal low velocity anomalies which are consistent with fractured and altered zones mapped at surface or sampled by the borehole cores. The three-dimensional maps of the distribution of P- and S-wave reveal the internal distribution of fractured, altered volumes and the unaltered, unfractured ones. The former features relatively high values of Poisson's ratio ($\sigma > 0.25$) and the latter relatively features low values ($\sigma < 0.25$). This correlation can be done because in volumes consistent of a single rock the variations of σ are related to pore space, fracturing and fluid content. A detailed characterization of the physical properties of a granitic pluton, including a three dimensional reconstruction of the fractures network and its surrounding are obtained by high resolution seismic tomography of P- and S-waves.

Acknowledgements

This research has been partially funded by the Spanish readioactive waste managing company (ENRESA), the European Community under contract FP6-516514, the Spanish Ministry of Education and Science grant MEC CGL2004-04623/BTE and the Generalitat of Catalunya grant 2005SGR00874. This manuscript has benefited from the comments of two anonymous reviewers. A previous version was commented by Albert Tarantola and Robert Hawman.

References

Aki, K., Richards, P.G., 1980. Quantitative seismology: theory and methods, vol. 1. Freeman & Co, New York. 557 pp.

Aki, K., Christofferson, A., Huseby, E., 1975. Three dimensional seismic velocity anomalies in the crust and the upper mantle under the USGS California seismic array. EOS Trans. Am. Geophys. Union, vol. 54, pp. 1145–1146.

Azaria, A., et al., 2000. 3-D seismic tomography survey at a groundwater contamination site. EOS 81 (F876).

Benz, H.M., Smith, R.B., 1984. Simultaneous inversion for lateral velocity variations and hypocenters in the Yellowstone region using earthquake and refraction data. Journal of Geophysical Research 89-B2, 1208–1220.

Benz, H.M., et al., 1996. Three-dimensional P and S wave velocity structure of Redoubt Volcano, Alaska. Journal of Geophysical Research 101-B4, 8111–8128.

Berge, P.A., Fryer, G.J., Wilkens, R.H., 1992. Velocity-porosity relationships in the upper oceanic crust: theoretical considerations. Journal of Geophysical Research 97-B11, 15239–15254.

Bishop, T.N., Bube, K.P., Cutler, R.T., Langan, R.T., Love, P.L., 1985. Tomographic determination of velocity and depth in laterally varying media. Geophysics 50, 903–923.

Carbonell, R., Smithson, S., 1994. Joint inversion of reflected PP, SS, and converted PS/SP travel times for crustal structure. Bulletin of the Seismological Society of America 84, 1889–1902.

Carbonell, R., Gallart, J., Pérez-Estaún, A., 2002. Modelling and imaging the Moho transition: the case of the southern Urals. Geophysical Journal International 149 (1), 134–148.

Carmichael, R., 1982. Handbook of physical properties of rocks, vol. II. CRC Press, Boca Raton, Florida.

Castagna, J., Backus, M.M., 1993. Offset-dependent reflectivity — theory and practice of AVO analysis. Society of Exploration Geophysicist, Tulsa, OK., USA.

Castro, A., 1986. Structural pattern and ascent model in the central Extremadura batholit, hercynian belt, Spain. Journal of Structural Geology 8, 635–645.

Chiu, S.K.L., Kanasewich, E.R., Phadke, S., 1986. Three dimensional determination of structure and velocity by seismic tomography. Geophysics 51–8, 1559–1571.

Christensen, N.I., Fountain, D.M., 1975. Constitution of the lower continental crust based on experimental studies of seismic velocities in granulites. Geological Society of America Bulletin 86 (2), 229–236.

Crampin, S., 1985. Evaluation of anisotropy by shear-wave splitting. Geophysics 50 (1), 142–152.

Crampin, S., Booth, D.C., 1989. Shear-wave splitting showing hydraulic dilation of pre-existing joints in granite. Scientific Drilling 1, 21–26.

Dawson, P.B., Chouet, B.A., Okubo, P.B., Villaseñor, A., Benz, H. M., 1999. Three dimensional velocity structure of the Kilauea Caldera, Hawaii. Geophysical Research Letters 26 (18), 2805–2808.

Escuder-Viruete, J., Carbonell, R., Jurado, M.J., Marti, D., Perez-Estaun, A., 2001. Two-dimensional geostatistical modeling and prediction of the fracture system in the Albala Granitic Pluton, SW Iberian Massif, Spain. Journal of Structural Geology 23 (12), 2011–2023.

Escuder-Viruete, J., Carbonell, R., Marti, D., Jurado, M.J., Perez-Estaun, A., 2003a. Architecture of fault zones determined from outcrop, cores, 3-D seismic tomography and geostatistical modeling: example from the Albala Granitic Pluton, SW Iberian Variscan Massif. Tectonophysics 361 (1–2), 97–120.

Escuder-Viruete, J., Carbonell, R., Marti, D., Perez-Estaun, A., 2003b. 3-D stochastic modeling and simulation of fault zones in the Albala granitic pluton, SW Iberian Variscan Massif. Journal of Structural Geology 25, 1487–1506.

Flecha, I., Marti, D., Escuder Viruete, J., Carbonell, R., Pérez-Estaún, A., 2004. Imaging low velocity anomalies with the aid of seismic tomography. Tectonophysics 388, 225–238.

Goff, J.A., Holliger, K., 1999. Nature and origin of upper crustal seismic velocity fluctuations and associated scaling properties: combined stochastic analyses of KTB velocity and lithology logs. Journal of Geophysical Research 104, 13169–13182.

Gorbatov, A., Widiyantoro, S., Fukao, Y., Gordeev, E., 2000. Signature of remnant slabs in the North Pacific from P-wave tomography. Geophysical Journal International 142, 27–36.

Hawley, B.W., Zandt, G., Smith, R.B., 1981. Simultaneous inversion for hypocenters and lateral velocity variations: an iterative solution with a layered model. Journal of Geophysical Research 86-B8, 7073–7086.

Hilterman, F., Schuyver, C.V., Sbar, M., 2000. AVO examples of long-offset 2-D data in the Gulf of Mexico. The Leading Edge 19, 1200–1213.

Hole, J.A., 1992. Nonlinear high-resolution three dimensional seismic travel time tomography. Journal of Geophysical Research 97-B5.

Hole, J.A., Zelt, B.C., 1995. 3-D finite-difference reflection travel times. Geophysical Journal International 121, 427–434.

Ji, S., Wang, Q., Xia, B., 2002. Handbook of seismic properties of minerals, rocks and ores. Polytechnic International Press, Montreal.

Jones, A., Holliger, K., 1997. Spectral analyses of the KTB sonic and density logs using robust nonparametric methods. Journal of Geophysical Research 102, 18391–18403.

Kissling, E., 1988. Geotomography with local earthquake data. Reviews of Geophysics 26, 659–698.

Korenaga, J., Holbrook, W.S., Kent, G.M., Kelemen, P.B., Detrick, R.S., Larsen, H.C., Hopper, J.R., Dahl-Jensen, T., 2000. Crustal structure of the southeast Greenland margin from joint refraction and reflection seismic tomography. Journal of Geophysical Research 105 (B9), 21591–21614.

Lynn, H.B., Simon, K.M., Bates, C.R., 1996a. Correlation between P-wave AVOA and S-Wave traveltime anisotropy in a naturally fractured gas reservoir. The Leading Edge 15 (8), 931–935.

Lynn, H.B., Simon, M., Bates, R., van Dok, R., 1996b. Azimuthal anisotropy in P-wave 3-D (multiazimuth) data. The Leading Edge 15 (8), 923–928.

Madrussani, G., Böhm, G., Vesnaver, A., Schena, G., 1999. Tomographic detection of cavities in mines for acid drainage control. European Journal of Environmental and Engineering Geophysics 3, 115–130.

Martí, D., 2004. Caracterización sísmica de un medio cristalino fracturado, Ph. D. Thesis, Institute of Herat Sciences "Jaime Almera", Barcelona, 2004.

Martí, D., Carbonell, R., Tryggvason, A., Escuder, J., 2002a. Calibrating 3D tomograms of a granitic pluton. Geophysical Research Letters 29 (17), 1834, doi:10.1029/2001GL012942.

Martí, D., Carbonell, R., Tryggvason, A., Escuder, J., Pérez-Estaún, A., 2002b. Mapping brittle fracture zones in 3 dimensions: high resolution travel time seismic tomography in a granitic pluton. Geophysical Journal International 149, 95–105.

Milligan, P.A., Rector, J.W., 2000. 3-D velocity imaging in the shallow subsurface using multi-well, multi-offset, VSP data: a case study from the Lawrence Livermore National Laboratory site. Journal of Environmetal and Engineering Geophysics 5 (1), 27–37.

Morey, D., Schuster, G.T., 1999. Palaeoseismicity of the Oquirrih fault, Utah from shallow seismic tomography. Geophysical Journal International 138, 25–35.

Mukerji, T., Mavko, G., 1994. Pore fluid effects on seismic velocity in anisotropic rocks. Geophysics 59-2, 233–244.

Nolet, G., 1985. Solving or resolving inadequate and noisy tomographic systems. Journal of Computational Physics 61, 463–482.

Nolet, G., 1993. Solving large linearized tomographic problems. In: Hall, C. (Ed.), Seismic tomography: theory and practice. London.

Nur, A., 1971. Effects of stress on velocity anisotropy in rocks with cracks. Journal of Geophysical Research 76, 2022–2034.

Paige, C., Saunders, M., 1982. LSQR: an algorithm for sparse linear equations and sparse least squares. ACM Transactions on Mathematical Software 8, 43–71.

Pavlis, G.L., Booker, J.R., 1980. The mixed discrete-continuous inverse problem: application to the simultaneous determination of earthquake hypocenters and velocity structure. Journal of Geophysical Research 85-B9.

Sanderson, D., Roberts, S., McGowan, J., Gumiel, P., 1991. Hercynian transpressional tectonics at the southern margin of the Central-Iberian zone, West Spain. Journal of the Geological Society (London) 148, 893–899.

Sallarès, V., Charvis, P., Flueh, E.R., Bialas, J., 2003. Seismic structure of Cocos and Malpelo Ridges and implications for hot spot-ridge interaction. Journal of Geophysical Research 108 (B12), 2564, doi:10.1029/2003JB002431.

Takahashi, T., Imayoshi, T., Takeda, T., 2001. Borehole seismic characterization of a heterogeneous rock. International Journal of Rock Mechanics and Mining Sciences 38, 851–857.

Tarantola, A., 1987. Inverse problem theory: methods for data fitting and model parameter estimation. Elsevier Science, New York. 613 pp.

Tarantola, A., Valette, B., 1982a. Generalized nonlinear inverse problems solved using the least squares criterion. Reviews of Geophysics and Space Physics 20-2, 219–232.

Tarantola, A., Valette, B., 1982b. Inverse problems: quest for information. Journal of Geophysics 50, 159–170.

Thurber, C.H., 1993. Earthquake locations and three-dimensional crustal structure in the Coyote Lake Area, Central California. Journal of Geophysical Research 88-B10, 8226–8236.

Tryggvason, A., 1998. Seismic tomography. Inversion for P-and S-wave velocities, Ph. D. Thesis, Uppsala University, Uppsala.

Tryggvason, A., Rögnvaldsson, S., Flóvenz, O.G., 2002. Three-dimensional imaging of the P- and S-wave velocity structure and earthquake locations beneath Southwest Iceland. Geophysical Journal International 151, 848–866.

Vidale, J.E., 1990. Finite-difference calculation of traveltimes in three dimensions. Geophysics 55-5, 521–526.

Zelt, C.A., Barton, P.J., 1998. Three-dimensional seismic refraction tomography: a comparison of two methods applied to data from the Faeroe Basin. Journal of Geophysical Research 103 (4), 7187–7210.